Peer reviewed version

Link to published version (if available):
[10.1016/j.epsl.2017.12.012](#)

Link to publication record in Explore Bristol Research
PDF-document

University of Bristol - Explore Bristol Research
General rights

Collisional stripping of planetary crusts

Philip J. Carter[a,b,*], Zoë M. Leinhardt[a], Tim Elliott[c], Sarah T. Stewart[b], Michael J. Walter[c]

[a]*School of Physics, University of Bristol, H. H. Wills Physics Laboratory, Tyndall Avenue, Bristol BS8 1TL, UK*
[b]*Department of Earth and Planetary Sciences, University of California Davis, One Shields Avenue, Davis, CA 95616, USA*
[c]*School of Earth Sciences, University of Bristol, Wills Memorial Building, Queen's Road, Bristol BS8 1RJ, UK*

Abstract

Geochemical studies of planetary accretion and evolution have invoked various degrees of collisional erosion to explain differences in bulk composition between planets and chondrites. Here we undertake a full, dynamical evaluation of 'crustal stripping' during accretion and its key geochemical consequences. Crusts are expected to contain a significant fraction of planetary budgets of incompatible elements, which include the major heat producing nuclides. We present smoothed particle hydrodynamics simulations of collisions between differentiated rocky planetesimals and planetary embryos. We find that the crust is preferentially lost relative to the mantle during impacts, and we have developed a scaling law based on these simulations that approximates the mass of crust that remains in the largest remnant. Using this scaling law and a recent set of *N*-body simulations of terrestrial planet formation, we have estimated the maximum effect of crustal stripping on incompatible element abundances during the accretion of planetary embryos. We find that on average approximately one third of the initial crust is stripped from embryos as they accrete, which leads to a reduction of ∼20% in the budgets of the heat producing elements if the stripped crust does not reaccrete. Erosion of crusts can lead to non-chondritic ratios of incompatible elements, but the magnitude of this effect depends sensitively on the details of the crust-forming melting process on the planetesimals. The Lu/Hf system is fractionated for a wide range of crustal formation scenarios. Using eucrites (the products of planetesimal silicate melting, thought to represent the crust of Vesta) as a guide to the Lu/Hf of planetesimal crust partially lost during accretion, we predict the Earth could evolve to a superchondritic ^{176}Hf/^{177}Hf (3-5 parts per ten thousand) at present day. Such values are in keeping with compositional estimates of the bulk Earth. Stripping of planetary crusts during accretion can lead to detectable changes in bulk composition of lithophile elements, but the fractionation is relatively subtle, and sensitive to the efficiency of reaccretion.

Keywords: Planet formation, Terrestrial planets, Impact erosion, Planet composition, Accretion, Crust.

1. Introduction

Terrestrial planets are thought to form from the accumulation of planetesimals into planetary embryos, followed by a period in which these embryos undergo giant impacts to form a final system of planets (e.g. Morbidelli et al., 2012). Accretion of planetesimals onto larger bodies is a key process during both intermediate and late stages of planet formation, but this process is not one of monotonic growth. The collisions experienced by the planets as they grow can also lead to loss of material and the final composition of a planetary body can be influenced by preferential erosion of chemically distinct layers (e.g. Carter et al., 2015).

Crusts are expected to contain a significant fraction of planetary incompatible element budgets (elements that are concentrated during magmatic processes because they more strongly partition into the melt than residual solid during partial melting), and it has previously been suggested that preferential removal of the outer crustal layers of planetary building blocks alter bulk compositions (e.g. Greenwood et al., 2005; O'Neill and Palme, 2008; Boujibar et al., 2015; Jellinek and Jackson, 2015). Since there is ample evidence of the early differentiation of planetesimals (e.g. Lugmair and Shukolyukov, 1998; Srinivasan et al., 1999; Bizzaro et al., 2005; Amelin, 2008; Kruijer et al., 2014), collisional erosion is an obvious means of removing the chemically distinct outer layers of growing planets. Several studies have previously demonstrated that collisions during accretion can

---

influence the major element compositions of the resulting objects (e.g. Marcus et al. 2009, 2010; Bonsor et al. 2015; Carter et al. 2015; Dwyer et al. 2015), but most of the work on individual collision outcomes has not focused on heterogeneous colliders (e.g. Leinhardt and Stewart, 2012), or has considered only giant impacts (Marcus et al., 2009, 2010). Moreover these studies have not quantified the budgets of important trace elements[1] used to characterise planetary bodies.

The modification of planetary compositions during growth has consequences for the long-standing paradigm that primitive meteorites, chondrites, represent the building blocks of planets. Chondritic ratios of cosmochemically refractory elements (elements with high condensation temperatures in a hydrogen-rich environment), such as the rare earth elements, have been taken to provide a robust bulk planetary reference. Yet, some doubt has been cast on the reliability of this approach given the possibility that the Earth has non-chondritic ^{142}Nd/^{144}Nd (Boyet and Carlson, 2005). Proposed means to account for the terrestrial ^{142}Nd/^{144}Nd include: the Earth is made from chondrites different to those in our current collection (e.g. Huang et al., 2013; Burkhardt et al., 2016), the Earth's mantle is incompletely sampled (e.g. Boyet and Carlson, 2005; Labrosse et al., 2007), or the Earth accreted from differentiated bodies that had experienced prior collisional erosion (e.g. Bourdon et al., 2008; O'Neill and Palme, 2008). Since ^{142}Nd is the daughter of the extinct radioisotope ^{146}Sm (half life ~100 Myr, Meissner et al. 1987), a reservoir enriched in Sm relative to Nd (i.e. incompatible element depleted) early in the evolution of the solar system (within the first 100 Myr) would evolve into a reservoir with elevated ^{142}Nd/^{144}Nd. Whilst the idea that the Earth accreted from distinct material has recently gained significant traction (see also Bouvier and Boyet, 2016) as a preferred explanation for super-chondritic terrestrial ^{142}Nd/^{144}Nd, recent dynamical models have underscored the potential for collisional modification of bulk planetary compositions during accretion (e.g. Bonsor et al., 2015; Carter et al., 2015), at least for readily fractionated materials. Here we specifically investigate the importance of such collisional losses from differentiated bodies for the ratios of key refractory, lithophile element isotopes (Sm-Nd, Lu-Hf).

1.1. Previous work

Marcus et al. (2009) presented simulations of giant impacts onto Earth and super-Earth sized bodies us-

ing differentiated impactors with Earth-like composition and masses in the range 0.25–10 $M_\oplus$ (where $M_\oplus$ is the mass of the Earth). As well as examining the catastrophic disruption criteria, they derived a scaling law for the change in bulk composition due to mantle stripping, demonstrating that the iron-to-silicate ratio of the largest remnant increases with increasing impact energy. That work was extended to ice-rock planets in Marcus et al. (2010).

Leinhardt and Stewart (2012) used the results of a variety of previous impact simulations (including Marcus et al. 2009) and conducted new *N*-body simulations of smaller (homogeneous) planetesimal collisions, using 10 km radius targets, to determine the effects of collision parameters on collision outcome. They derived scaling laws to describe the size and velocity distribution of the collision remnants (see also Leinhardt et al. 2015). This work demonstrated that the collision outcome is velocity dependent, allowing correction for the impact angle and mass ratio.

We have previously applied the Marcus et al. (2009) mantle stripping law and the state-of-the-art collision model from Leinhardt and Stewart (2012) and Leinhardt et al. (2015) to examine the changes in bulk composition during accretion of planetary embryos using high resolution *N*-body simulations (Bonsor et al., 2015; Carter et al., 2015). These simulations of the intermediate stages of planet formation, from ~100 km planetesimals to planetary embryos, explored two contrasting dynamical scenarios: a calm disc unperturbed by giant planets, and the dynamically hot Grand Tack model (Walsh et al., 2011). We found that significant compositional change can occur, in terms of core/mantle ratio, in growing planetesimals, especially in dynamically hot protoplanetary discs (Carter et al., 2015).

Here we explore the effects of collisions on the crusts of planetesimals by conducting a new set of impact simulations, and explore the implications for planetary compositions by applying scaling laws to previous *N*-body simulations of planet formation. We begin by describing the impact simulations, and the post-processing of *N*-body simulations to examine crust stripping during accretion (section 2). We present the results of the impact simulations in section 3.1 and the results of the post-processing in section 3.2, then discuss these results in section 4.

2. Numerical Methods

2.1. Hydrodynamic modelling

We simulated collisions between planetesimals and embryos using a version of the GADGET-2 smoothed

---

[1]Trace elements are defined as having concentrations <1000 ppm

particle hydrodynamics (SPH) code (Springel, 2005) modified for planetary collision calculations. This modified version of GADGET-2 calculates thermodynamic quantities by interpolating tabulated equations of state, for details see Marcus et al. (2009), Marcus et al. (2010), and Ćuk and Stewart (2012). As in previous studies (Marcus et al., 2009; Ćuk and Stewart, 2012; Lock and Stewart, 2017), we modelled the silicate layers and metallic cores of terrestrial planet embryos as pure forsterite and pure iron using tabulated equations of state obtained from the M-ANEOS model (Melosh 2007; these tables are available in the online supplement to Ćuk and Stewart 2012).

The initial differentiated planetesimals were comprised of 22 wt% iron and 78 wt% forsterite (this smaller iron core compared to Marcus et al. (2009) is consistent with chondritic building blocks). The bodies were initialised with a simple temperature profile approximating the state of planetesimals in the first few million years of evolution. Since the planetesimals are differentiated they should have undergone large-scale melting, and so, based on the melting model from Hevey and Sanders (2006), we set the temperature to 1850 K from the centre to $0.8R$ (where R is the radius of the body), dropping linearly to 300 K at the surface.

The bodies were then evolved through two equilibration steps each lasting 10 hours. Because the initial density and temperature distribution are not perfectly in gravitational equilibrium, large particle motions are induced as the body evolves under self-gravity. Thus, to accelerate convergence to equilibrium, particle velocities are damped by a factor of 50% per time step during the first 10 hour period. Without damping, these particle velocity perturbations can generate strong shocks that disturb the desired thermal profile (sometimes in a dramatic fashion). In the second equilibration phase the body evolves under self-gravitational forces (without additional damping) towards a hydrostatic profile. In many cases particle motions during equilibration led to a single particle reaching escape velocity. The state of a planetesimal of mass $1 \times 10^{-5}\,M_\oplus$ after equilibration is shown in Figure 1. This equilibration procedure does not significantly alter the temperature profile of the body.

We used target masses of $1 \times 10^{-5}\,M_\oplus$, $5 \times 10^{-5}\,M_\oplus$, $1 \times 10^{-3}\,M_\oplus$, and $1 \times 10^{-1}\,M_\oplus$, mostly comprised of 2×10^4 particles; more extreme mass ratios require higher resolution in order for the projectile to be well resolved. For projectile/target mass ratios smaller than 0.1 we used targets comprised of 2×10^5 particles. A subset of collisions were run with ten times as many particles to check sensitivity to resolution, producing equivalent

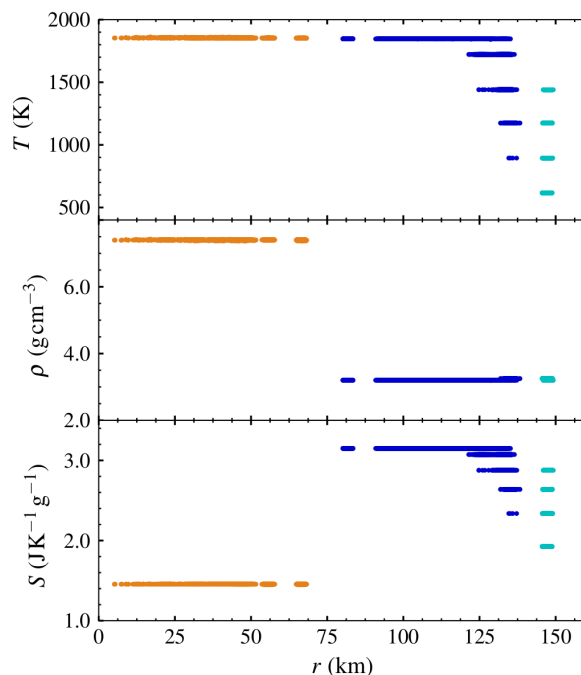

Figure 1: Radial temperature, density and specific entropy structure of a $10^{-5}\,M_\oplus$ planetesimal after gravitational equilibration. The orange and blue points represent particles in the iron core, and forsterite mantle respectively, the cyan points indicate the crust-tracing silicate particles.

results.

We explored mass ratios of 0.01, 0.02, 0.05, 0.1, 0.2, 0.3, 0.4, 0.5 and 1.0, with the projectile having the same mass per particle as the target. Impact parameters of 0.1, 0.25, 0.4, 0.5, and 0.8 were selected to provide good coverage of the parameter space of collisions that occurred in the simulations of Carter et al. (2015). Impact velocities ranged from 0.8 to 15 times the mutual escape velocity[2], v_{esc}. The full list of simulations is available in the supplementary material (Tables S1 and S2).

In addition to the separate iron core and forsterite mantle, the outer silicate layer of each body was tagged to represent the planetesimal's crust (see Figures 1 and 4). Although this material is labelled as crust, it is compositionally identical to the mantle for the dynamic calculations and we assume that the small differences in densities of real planetary crusts have minimal effect. This outer layer of SPH particles (4980–5370 particles for the standard resolution targets) may not fully resolve the crust, depending on the unknown thickness of the crust on such bodies, and so we assume some fraction of each surface particle represents crustal material (as in Marinova et al., 2008) and scale the crust mass accordingly. Ascribing distinct chemical characteristics to crustal material is only done in the post-processing stage (see section 2.2).

Bodies were initially separated by an additional projectile radius (i.e. the separation between the body centres in the direction of motion was set to $R_{targ} + 2R_{proj}$) such that they were not already in contact at the start of the run. Most simulations were run for at least 24 hours (model time within the simulation) to allow reaccumulation of debris onto the largest remnant.

The mass of the largest remnant following each collision was calculated using the same approach used by Marcus et al. (2009). The potential and kinetic energies of all particles were calculated with respect to the potential minimum, and the centre of mass for all bound particles calculated. This process was repeated on unbound particles until the remnant mass converged. The remnant mass was considered unreliable if it consisted of fewer than 100 particles, in these cases the impact was ignored in further analyses (and no mass is recorded in Table S1). The same approach was followed to identify the second largest remnant, ignoring particles already identified as bound to the largest remnant. The mass of the resulting iron core was found simply from the mass of iron particles in the largest remnant. Since the num-

ber, and hence mass, of 'crust' particles in a body depends on its size, we converted the number of crust particles in the remnant to a mass by assuming the initial bodies each had a crust mass of 15% of the body's total mass (based on observations of Vesta, see section 2.2), and scaling the crust mass fraction of the outer layer particles accordingly.

Finally, the catastrophic disruption threshold, Q'^*_{RD} (the specific energy required to disperse half of the total mass), was estimated by fitting a straight line (according to the universal law from Leinhardt and Stewart 2012) to the mass of the largest remnant as a function of the specific energy of the impact, Q_R (calculated using the reduced mass), for each group of target mass, mass ratio and impact parameter. Simulations with largest remnants smaller than 0.3 times the total mass were excluded from these calculations, as these may be in the supercatastrophic regime, and would thus deviate from the linear relation. In the case of hit-and-run impacts the same procedure was followed using the mass of the second largest remnant, M_{slr}, compared to the projectile to calculate $Q^{\dagger'*}_{RD}$ (where the $\dagger$ is used to indicate the reverse impact onto the projectile, see Leinhardt and Stewart 2012).

2.2. Crustal composition evolution

In order to examine the consequences of collisions for the compositions of accreting planets, we used the crustal loss scalong law inferred from the SPH simulations (section 3.1) to post-process the same set of high resolution N-body simulations used to inform the choice of SPH simulations, those from Carter et al. (2015). Each body was assigned initial crust and mantle compositions as described below, and based on the predicted crust and mantle loss (or gain) as a function of specific impact energy the new crust and mantle masses and compositions of bodies were calculated after each collision. In hit-and-run collisions the target is assumed to be unchanged, but stripping of the projectile's crust is calculated in the same way, using the specific energy of the reverse impact (see Leinhardt and Stewart 2012). In the disruption regime, for impacts below Q'^*_{RD} the second largest remnant is assumed to come from the projectile, above Q'^*_{RD} it is assumed both the largest and second largest remnants are fragments of the target, as indicated by the SPH impacts.

We track the crustal compositions of the elements of interest, namely Sm, Nd, Lu, Hf, Th and U. This suite of incompatible, refractory lithophile elements allows us to track the isotopic evolution of the Sm-Nd and Lu-Hf systems in addition to the fate of major heat-producing elements. We use Vesta as a suitable ana-

---

[2] $v_{esc} = \sqrt{2GM_{Tot}/R}$, where M_{Tot} is the sum of the target and projectile masses, and R is the radius of a sphere of mass M_{Tot} with the same bulk density as the target (Leinhardt and Stewart, 2012).

logue for intermediate sized planetesimals, and consider three different approaches for setting crustal compositions. a) We calculate a 'model' crustal composition based on existing petrological studies of Vesta (Ruzicka et al., 1997; Mandler and Elkins-Tanton, 2013) and appropriate melt-solid partition coefficients (D, see Table 1) taken from Workman and Hart (2005). b) We use analyses of eucritic meteorites (Blichert-Toft et al., 2002; Barrat et al., 2000), which are believed to be derived from Vesta, to determine the crustal composition. c) The consequences of more extreme differentiation experienced in larger bodies during later accretion are assessed with a 'KREEP-rich' lunar crust. This numerically combines an anorthosite outer layer with the potassium, rare earth element and phosphorous rich (KREEP) residuum of lunar magma ocean crystallisation (e.g. Snyder et al., 1992). Our empirical crustal compositions are reported in Table 1 as 'eucritic' and 'KREEP-rich' respectively. For the model and eucritic crusts we assume a silicate melt fraction of 20% (i.e. the crust mass is 20% of the silicate mass of the body, ~15% of the total mass), which is appropriate for the estimated fraction of Vesta's eucritic crust (e.g. Mandler and Elkins-Tanton, 2013), and for the KREEP-rich crust we assume the crust is 5.04% of the silicate mass, consistent with our calculated lunar crust. Further details of how we derive these composition are given in Appendix A.

For each of these 3 composition models we explore two scenarios of crustal evolution: 1) after each collision any remaining crust on each body is fully mixed with the residual mantle, and a new crust is formed by melting of this new mantle (which includes any mantle or crust accreted from an impactor); the composition of both crust and mantle can change as a result of the collision; 2) any crust remaining is assumed to redistribute across the planetesimal, but no new crust is created to replace that which was lost (both mantle and crust retain their initial composition).

Initially, and in the case of the first evolution scenario each time new crust is produced, the required mass of crust matching the empirical composition (or containing all of a species left in the body if it is already so depleted that there is not enough left to match the composition) is formed according to mass-balance calculations (eucritic and KREEP-rich crusts), or the crust composition is set via element partitioning between the mantle and melt according to measured partition coefficients (model crust).

Since this is a post-processing calculation using N-body simulations that did not track crust, it is not possible to follow the long-term (over multiple orbits) fate of
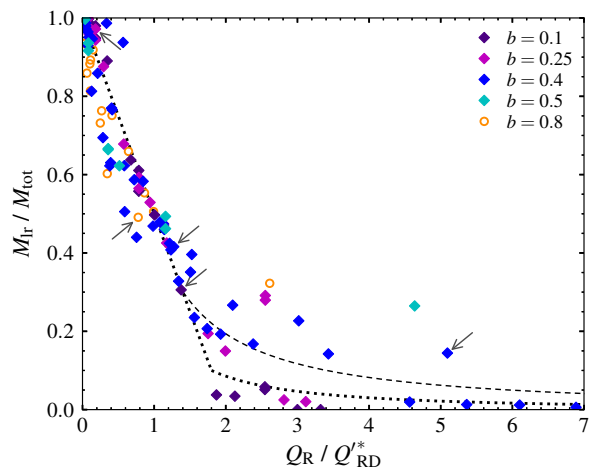

Figure 2: Normalised largest remnant mass vs. normalised specific impact energy. The symbol colour denotes the impact parameter. The dotted line is the universal law and, beyond the break in slope at a specific energy of 1.8, the supercatastrophic disruption power law from Leinhardt and Stewart (2012). The dashed line (also from Leinhardt and Stewart 2012) represents laboratory measurements of basalt disruption from Fujiwara et al. (1977). The open circles are hit-and-run collisions for which M_{slr}/M_{proj} vs $Q_R^{\dagger}/Q_{RD}^{\dagger'*}$ (see text) is plotted. The arrows indicate collisions shown in detail in Figure 4.

stripped crustal material that is initially unbound from the largest remnant, but is still bound to the star. Thus we calculate the end-member scenario in which we neglect the chemical consequences of reaccretion of this material.

3. Results

3.1. Simulation results

Figure 2 shows the mass of the largest remnant, M_{lr}, against the specific impact energy relative to the catastrophic disruption threshold. The dotted line in this figure represents the 'universal law' for the mass of the largest remnant and the power law for the supercatastrophic regime from Leinhardt and Stewart (2012). Our results show excellent agreement with the Leinhardt and Stewart (2012) model in the accretion and erosion regimes, despite the different methods and impactor sizes, and good agreement with significant scatter in the supercatastrophic regime. Similar results were seen by Marcus et al. (2009) (their impact energies were all less than two times the catastrophic disruption threshold). It is worth recalling that the targets simulated in this work fall between the size regimes explored by Leinhardt and Stewart (2012) and Marcus et al. (2009).

The mass fraction of the iron core of the largest remnant as a function of specific impact energy is shown
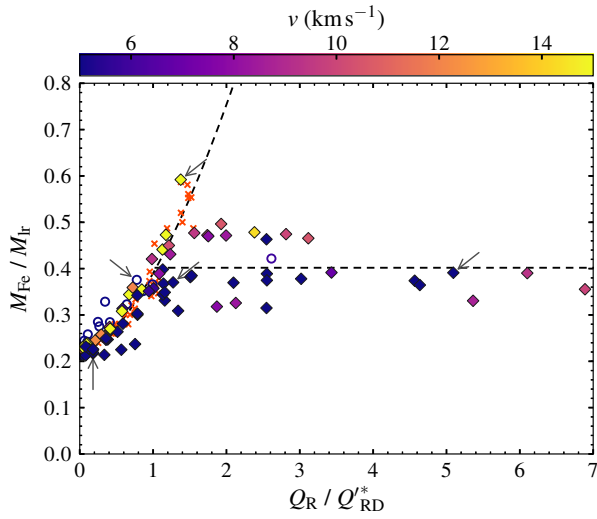
Figure 3: Iron fraction for the largest remnant vs. normalised specific impact energy. Diamonds indicate non-grazing collisions and open circles indicate hit-and-run collisions from this work, and are coloured according to impact velocity; red crosses (not representative of velocity) are from Marcus et al. (2009), scaled down to match the core fraction used in this work. The dashed curve is a scaled down version of the fit from Marcus et al. (2009). The horizontal dashed line represents a fit to the iron fraction from this study only above a scaled impact energy of 1.0. The arrows indicate collisions shown in detail in Figure 4. For hit-and-run collisions the iron fraction of the second largest remnant and $Q_R^\dagger / Q_{RD}^{\dagger\prime*}$ are plotted.

in Figure 3. The dashed curve in this figure is equation 3 from Marcus et al. (2009), scaled by the ratio of the initial core fraction used in this work, 0.22, to the initial core fraction used in Marcus et al. (2009), 0.33. Our results show remarkable consistency with this model despite the lower core fraction.

At low energies the Marcus et al. (2009) model is in excellent agreement with our results, however, we find that the core mass fraction generally reaches a plateau at a value of approximately 0.4. The second collision sequence shown in Figure 4 helps to illustrate this: the mantle (and crust) on the lower left of the target's core largely remain behind the remaining core, later becoming a major component of the remnant's mantle.

The crust mass fraction of the largest remnant as a function of scaled specific impact energy is shown in Figure 5. Since the increasing core fraction (Figure 3) requires a preferential loss of mantle in collisions (see also Marcus et al., 2009; Bonsor et al., 2015; Carter et al., 2015), it is unsurprising that we also find a preferential loss of crust. Again we see that in many cases the crust mass fraction levels out above specific impact energies of $\sim Q_{RD}^{\prime*}$ as the antipode crust is 'protected' along with the mantle.

Figure 5 reveals that higher velocity impacts lead to lower crust fractions; this can also be seen by comparing the low and high velocity erosive collisions shown in Figure 4. We find a good fit to the crust fraction of the largest remnant, $f_{crust,lr}$, with linear relations, dividing the two regimes at a velocity of 9 km s^{-1}, such that

$$f_{crust,lr} = \begin{cases} f_{crust,i} \left(1 - 0.47 \left[\frac{Q_R}{Q_{RD}^{\prime*}} \right] \right) & \text{if } \frac{Q_R}{Q_{RD}^{\prime*}} < 0.85 \\ & \text{or } v > 9 \text{ km s}^{-1}, \\ 0.60 \, f_{crust,i} & \text{otherwise,} \end{cases}$$

(1)

where $f_{crust,i}$ is the initial crust mass fraction.

Similarly, the core fraction of the largest remnant can be expressed as

$$\frac{M_{Fe}}{M_{lr}} = \begin{cases} f_{Fe,i} \left(1 + 0.76 \left[\frac{Q_R}{Q_{RD}^{\prime*}} \right]^{1.65} \right), & \text{if } \frac{Q_R}{Q_{RD}^{\prime*}} < 1.04 \\ & \text{or } v > 9 \text{ km s}^{-1}, \\ 1.82 \, f_{Fe,i} & \text{otherwise,} \end{cases}$$

(2)

where $f_{Fe,i}$ is the initial core mass fraction.

3.2. Crust stripping throughout accretion

We have used the crust stripping law determined in the previous section to compare initial compositions with chondritic ratios of refractory lithophile elements
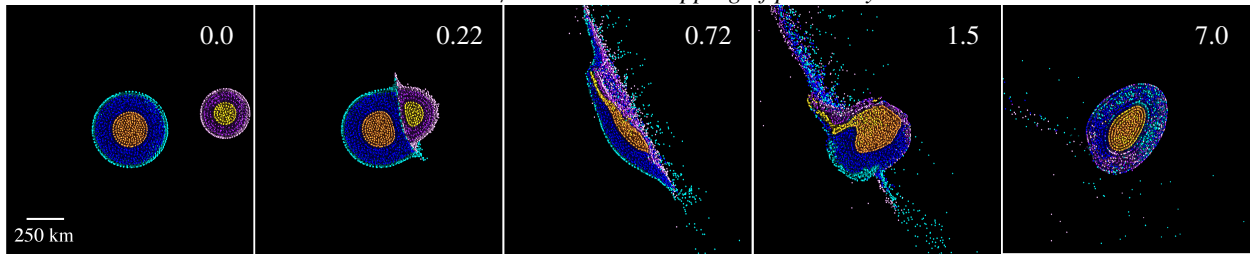
(a) Partial accretion collision between planetesimals with radii of 250 km and 170 km (mass ratio 0.3), at an impact velocity of 0.5 km s^{-1} (1.2 v_{esc}) and impact parameter of 0.25.
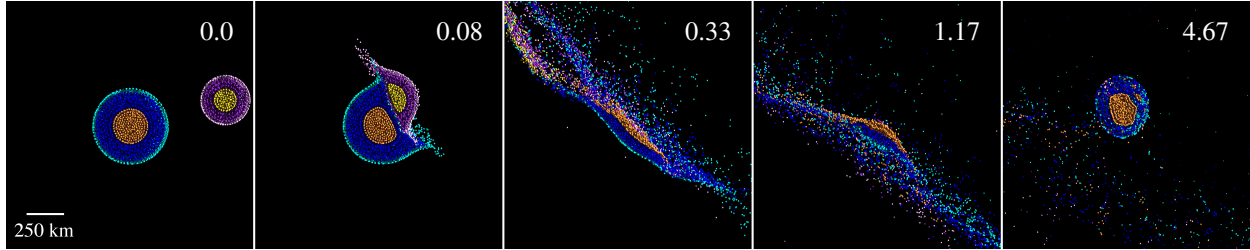
(b) Erosive collision between planetesimals with radii of 250 km and 170 km (mass ratio 0.3), at an impact velocity of 1.9 km s^{-1} (4.5 v_{esc}) and impact parameter of 0.4.
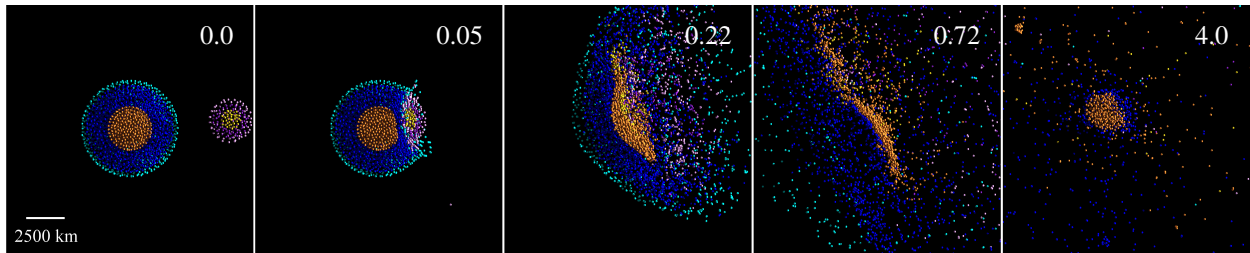
(c) Erosive collision between an embryo with radius of 3160 km and a planetesimal with radius 1470 km (mass ratio 0.1), at an impact velocity of 24.1 km s^{-1} (5 v_{esc}) and impact parameter of 0.1.
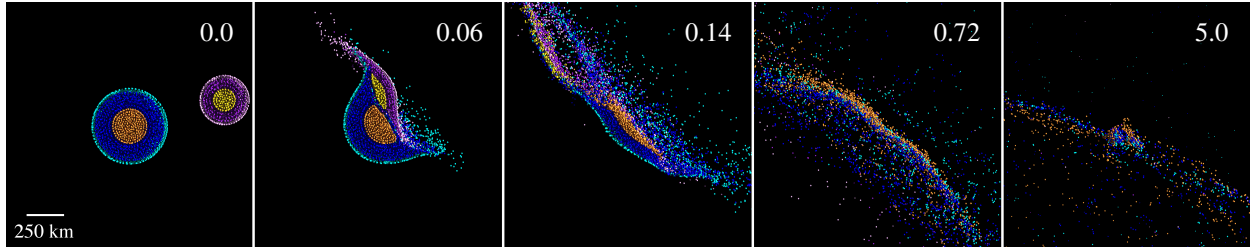
(d) Supercatastrophic disruption due to collision of planetesimals with radii of 250 km and 170 km (mass ratio 0.3), at a velocity of 3.8 km s^{-1} (9 v_{esc}) with an impact parameter of 0.4.
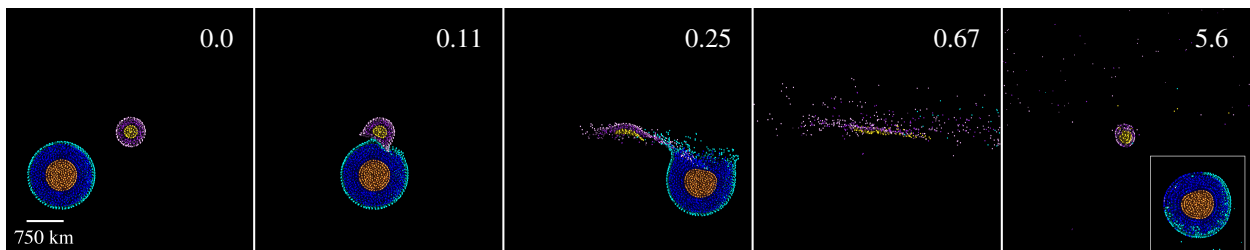
(e) Hit-and-run collision between planetesimals with radii of 680 km and 320 km (mass ratio 0.1), at a velocity of 3.2 km s^{-1} (3 v_{esc}) with an impact parameter of 0.8. The inset in the last panel shows the remnant of the target.

Figure 4: Time series of collisions showing several different outcomes. The numbers indicate the time in hours from the start of the simulation. The target's core, mantle and crust are coloured orange, blue and cyan; the projectile's are coloured yellow, purple and lilac. Only SPH particles below the equatorial *xy*-plane are shown. Each frame is centered on the largest remnant (or second largest in the hit-and-run case). Animations accompanying this figure are available in the supplementary material.
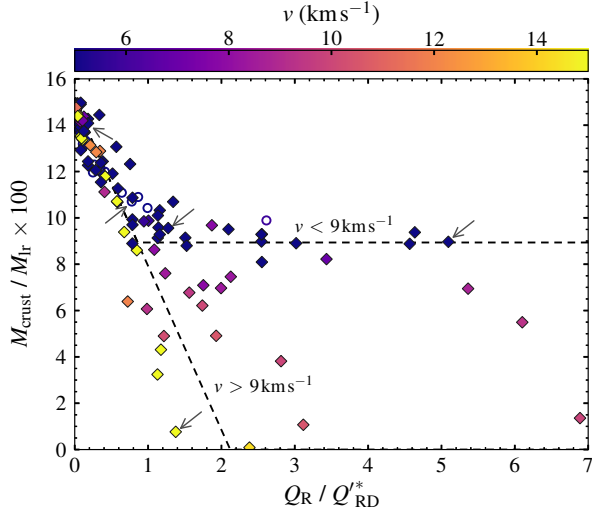
Figure 5: Crust mass fraction for the largest remnant vs. normalised specific impact energy. Points are coloured according to impact velocity, diamonds represent non-grazing collisions and open circles indicate hit-and-runs collisions. The dashed line corresponds to equation (1). The arrows indicate collisions shown in detail in Figure 4. For hit-and-run collisions the crust fraction of the second largest remnant and $Q_R^\dagger / Q_{RD}^{\prime\dagger*}$ are plotted.

Figure 6: Distribution of crust lost during accretion as a fraction of final embryo mass (for scenario 1, in which crust is replaced after each impact). The 20% melt we have used produces a crust ~15% of the body mass, as indicated by the dotted line.

Figure 7: Elemental abundances of collisionally processed embryos relative to initial compositions averaged across high resolution simulations from Carter et al. (2015) for both calm and Grand Tack simulations. The results for the eucritic crust (filled symbols), model crust (open symbols) and KREEP-rich crust (half-filled symbols) are shown (for scenario 2). The elements are not placed on a strict scale, rather they are spaced to reflect their incompatibilities (labelled by their bulk partition coefficients on the upper axis). The symbols represent the mean values, and the ranges indicate the 2σ width of the distribution. Note that the depletions for any particular embryo are correlated, such that an object showing the greatest depletion in one element will also display the greatest depletion in the other elements.

to that which would be predicted by our dynamical models. We applied the crust stripping model to each collision in a set of N-body simulations that represent the intermediate stages of terrestrial planet formation (Carter et al., 2015), and thus obtain the bulk silicate abundance of Nd, Sm, Lu, Hf, Th and U in the resulting planetary embryos (Mars mass and above).

The total mass of crust removed during the accretion of planetary embryos is shown in Figure 6. Here we only show results for scenario 1, where crust is assumed to be replaced after each impact and so loss is at a maximum. For scenario two the mass of crust lost is ~2–3% lower, however, embryos with the lowest mass loss experience approximately the same mass loss in either scenario. The majority of the collisions during the growth of embryos are either low energy accretional or hit-and-run impacts (Bonsor et al., 2015; Carter et al., 2015), so it is not surprising that planetesimals generally lose crust equivalent to only a third to a half of their initial crust mass (Figure 6). In some cases, particularly for the dynamically hot Grand Tack scenario, growing embryos can lose a mass of crust equivalent to their initial crust. It is important to note that this calculation assumes no reaccretion of stripped crust, and so geochemical calculations based on this loss represent the maximum change.

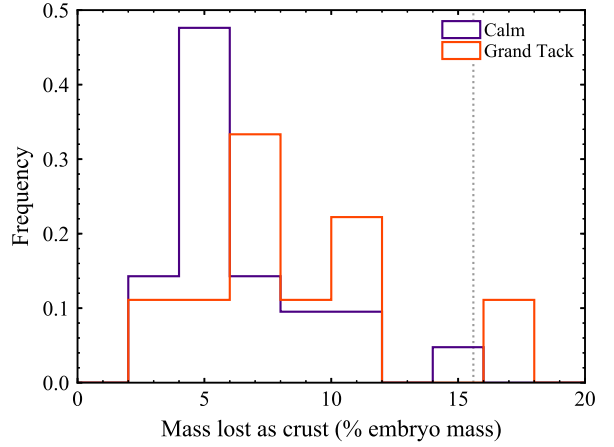The bulk abundance of each element in the final plan-

Table 1: Abundances and bulk partition coefficients, D, used for composition calculations, and resulting average embryo compositions (in scenario 2). Bulk silicate Vesta (BSV) abundances based on CI chondrite data from Palme and Jones (2003), partition coefficients taken from Workman and Hart (2005), eucrite composition from Blichert-Toft et al. (2002) and Barrat et al. (2000), and KREEP-rich composition based on a combination of an anorthosite outer layer Münker (2010) with a KREEP layer Warren (1989), see section 2.2. Details of the isotope ratio calculations are given in Appendix B.

| Element | BSV (ppm) | Eucrite (ppm) | KREEP (ppm) | $D^{\text{crystal/melt}}$ | Mean embryo abundance relative to BSV | | | | | |
| | | | | | model | | eucritic | | KREEP | |
					calm	GT	calm	GT	calm	GT
Nd	1.422	5.999	13.58	0.031	0.8148	0.7469	0.8243	0.7593	0.8996	0.8576
Sm	0.462	1.941	3.667	0.045	0.8235	0.7583	0.8250	0.7602	0.9164	0.8795
Lu	0.076	0.287	0.380	0.120	0.8592	0.8048	0.8431	0.7838	0.9473	0.9198
Hf	0.321	1.408	2.876	0.035	0.8174	0.7502	0.8173	0.7502	0.9057	0.8656
Th	0.089	0.377	1.638	0.001	0.7927	0.7181	0.8244	0.7594	0.8078	0.7377
U	0.023	0.103	0.454	0.0011	0.7928	0.7182	0.8167	0.7494	0.7965	0.7230
ϵ^{143}Nd	-	-	-	-	1.25	1.77	0.10	0.14	2.17	2.97
ϵ^{176}Hf	-	-	-	-	5.41	7.69	3.33	4.73	4.85	6.63
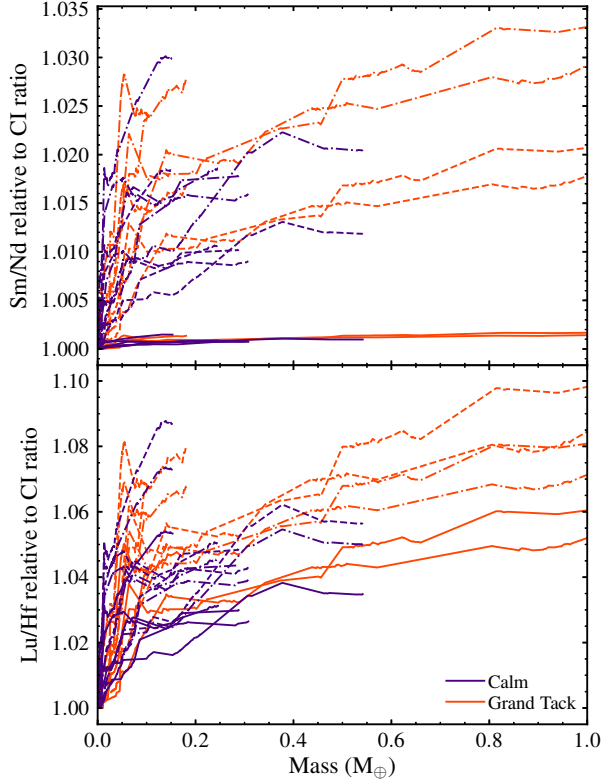
Figure 8: Evolution of Sm/Nd and Lu/Hf ratios of individual collisionally processed embryos for example calm and Grand Tack simulations from Carter et al. (2015). All embryos are shown at the same point in time, at which some have grown more massive than others. In both cases the fractionation is lower with a eucritic crust (solid lines) than with the model crust (dashed lines) or KREEP-rich crust (dot-dashed lines). Other simulations show similar results.

etary embryos compared to the initial composition is shown in Figure 7. Note that ranges shown reflect the variation across the sample of embryos, and the values for any particular embryo are correlated, such that an object showing the greatest depletion in one element will also display the greatest depletion in the other elements. There is little difference between the two scenarios for crustal loss we have tested, and so we show here only the result of the second scenario, in which no new crust is formed (a comparison between the two is available in the supplementary material, Figure S1). The elemental depletions do not correspond exactly to the mass of crust lost (Figure 6) as it is only loss of crust relative to mantle that controls the compositions considered here.

Assuming no reaccretion of lost crustal material, some 20% to 30% of the initial inventory of Th and U (key heat-producing elements) can be lost as a result of collisional accretion (Figure 7). The influence of accretional erosion on refractory element ratios is illustrated in more detail in Figure 8, which shows the evolution of the Sm/Nd and Lu/Hf ratios in planetary embryos. The choice of crustal composition has an important influence on the final Sm-Nd ratio in particular. This ratio is little changed for loss of eucritic crust, but is significantly perturbed for our model crust, where fractionation is controlled by mantle melting (principally by the partition coefficients of clinopyroxene) and also in our KREEP-rich crust. In a dynamically excited disk (Grand Tack model), an increase in the Sm/Nd ratio of up to 3% can be achieved. In all cases, Lu-Hf discernibly increases, and again the change is more marked for loss of our model or KREEP-rich crusts.

4. Discussion

4.1. SPH impact simulations

Both the core fraction and the crust fraction of the largest remnant split into two regimes above a specific impact energy approximately equal to Q'^*_{RD} (see Figures 3 and 5). For lower velocity impacts, the antipode does not reach escape velocity (at least for the combinations of impact geometry and energy explored), thus the mantle and crust near the antipode remain to be incorporated into the largest remnant. In disruptive impacts with velocities above about $9\,\mathrm{km\,s^{-1}}$, however, material near the antipode reaches sufficiently high velocities to be ejected (see Figure 4), and all of the original crust can be removed in high energy impacts. The iron fraction data from Marcus et al. (2009) show only the upper branch in which a higher mantle fraction is lost. The larger embryos and Earth-mass planets used in those simulations required rather higher impact velocities to reach specific energies above Q'^*_{RD}, and as such all fell into the antipode-ejection regime.

Close examination of Figures 3 and 5 suggests a transition region between the two regimes in a narrow velocity range between 9 and $\sim 12\,\mathrm{km\,s^{-1}}$. For the crust mass fraction (in the region between the two lines in the lower right part of Figure 5) this transition appears to be well ordered with impact velocity increasing as the lower 'branch' is approached. It is worth noting that in the simulations of the intermediate stages of planet formation from Carter et al. (2015), there are few impacts above the critical disruption threshold that reach sufficiently high velocities to enter the antipode-ejection regime. Since larger targets are unlikely to experience low velocity collisions that are capable of causing significant erosion, they are unlikely to fall into the plateau regime, and we expect neglecting the transition region and using only two separate branches to have a negligible effect.

Hit-and-run impacts match well to the 'universal law' (dashed line in Figure 2, Leinhardt and Stewart 2012), and both the core and crust mass fraction scaling laws when the reverse impact onto the projectile is considered (see Figures 2, 3 and 5). The target is almost unaffected in hit-and-run collisions (see Figure 4), its composition does not change significantly in any of the simulations, though there is a small amount of erosion of the target for higher velocity hit-and-run impacts (see Table S1). The remnant of the projectile generally shows slightly more scatter than the largest remnant of non-grazing impacts, but given the complexities of this regime the agreement is remarkable. It is worth noting, however, that the hit-and-run regime is less well explored than the non-grazing regime in this set of simulations.

Genda et al. (2015) identified a resolution dependence for SPH simulations of disruptive collisions, and suggested that it was necessary to use at least 5×10^6 particles in the target to obtain the value of the catastrophic disruption energy to an acceptable accuracy. Both the standard and higher resolutions used in this work (2×10^4 or 2×10^5 particles) are substantially lower than Genda et al.'s, however, the 10 times higher resolution checks show at most a 10% difference in M_{lr} (see Table S1), well within the scatter shown in Figure 2. It is worth noting that our results do show the same lower Q^*_{RD} at higher numerical resolution trend as seen by Genda et al. (2015), but our resolution tests demonstrate that our lower resolution is acceptably accurate.

4.2. Geochemical consequences of crust stripping

The chemical effects of crustal stripping shown in section 3.2 give realistic estimates of the maximum depletion in incompatible elements on the Earth. Unsurprisingly the dynamically hot Grand Tack scenario leads to a greater depletion of incompatible elements in planetary embryos. Figure 8 shows that changes in composition due to crust stripping are greatest when the embryos are small, with a large fraction of the loss of incompatible species occurring before the growing embryos reach Mars mass. Smaller bodies are easier to disrupt, and more likely to experience high specific energy collisions, thus crust (and mantle) are more easily removed from small planetesimals than larger embryos. It is expected that the giant impact stage will be dominated by accretion and hit-and-run events, with very few erosive impacts (Stewart and Leinhardt, 2012). This suggests that crust stripping is most important at earlier times, and that the final stages of evolution to fully formed planets will have a smaller effect on incompatible element compositions.

There is one significant simplification in the post processing model that should be considered: the lack of reaccretion of stripped crust. We have seen previously that reaccretion of eroded mantle and core material is important for the bulk composition of terrestrial planets (Carter et al., 2015). In Carter et al. mantle and core were tracked directly in the simulations, as was the composition of reaccreted material; whilst here we have post-processed the collisions to estimate the crust loss, a method which cannot track the composition for fragments beyond the second largest remnant. This precludes a direct comparison between the mantle stripping results from Carter et al. (2015) and the crust stripping estimated here.

As crust represents a very small fraction of the total mass it is possible that this material might be removed from the terrestrial planet region without substantial reaccretion. Whilst the nebular gas remains in the system small debris particles may be lost by spiralling into the star due to aerodynamic drag (Adachi et al., 1976), but could be reaccreted by growing planetary bodies before they are removed form the planet forming region. After the gas has been expelled, debris might grind down to particles small enough to be removed by photon pressure (e.g. Kobayashi and Tanaka, 2010), but it is unclear if this mechanism is efficient whilst accretion is ongoing. The fate of ejecta during planet formation is an important topic that requires further study. Nevertheless, we would expect at least some ejected crust material to be reaccreted, likely leading to a greater variation in compositions, but also a reduction in the average elemental depletions. This would work to reduce the compositional changes from the maximum values given in Figures 7 and 8, but we do not anticipate complete reaccretion onto the originating body as this would be inconsistent with the variation in iron content of planetary embryos seen in Carter et al. (2015).

Boujibar et al. (2015) suggested that the elemental disparity but isotopic similarity between the Earth and enstatite chondrites could be explained by collisional erosion of a Si-rich proto-crust. In order to match the high Mg/Si ratio of Earth's primitive upper mantle, they estimated that crust equivalent to >15% of the final planet mass would need to be removed. They also identify that this process must occur early as the Si enrichment of crust-forming melts decreases with increasing pressure (body size). The results of our simulations and post-processing suggest that proto-crust can be eroded by collisions during accretion, but the average mass of crust that is removed is a smaller fraction of the total planetary mass (6–9%) than required by Boujibar et al. (2015). The true discrepancy is larger since we assume a crustal melt fraction of 20% as opposed to the low degrees of melting (5-7%) needed by Boujibar et al. (2015) and this increases the mass of crustal loss in our scenario. Moreover, differentiation of planetary bodies occurs early whereas the melt compositions used by Boujibar et al. (2015) are based on a primitive enstatite chondrite starting composition. Melt compositions from highly reduced parent bodies that are present in the meteorite record, aubrites, are less Si-rich than the experimental melts of Boujibar et al. (2015). Such empirical crustal compositions would require a greater amount of crustal stripping to produce a terrestrial Mg/Si from an enstatite chondrite starting composition, and we think it unlikely that collisional erosion of crust can account for

this. However, collisions may play an important role in this regard if they cause vapour loss that results in compositional modification (Pringle et al., 2014; Hin et al., 2017).

O'Neill and Palme (2008) suggested that loss of an incompatible element enriched crust during accretion could leave Earth enriched in Sm realtive to Nd, and lead to a superchondritic $^{142}Nd/^{144}Nd$ for bulk Earth. Figure 8 reveals that using our model or KREEP-rich crust, accretional erosion can naturally lead to a Sm/Nd ratio several percent higher than the chondritic ratio. Since the evolution of planetary embryos considered here is expected to occur early (in the first few Myr of solar system evolution), well before ^{146}Sm is extinct, it is expected that the elevated Sm/Nd ratio would alter the $^{142}Nd/^{144}Nd$ ratio of the resulting planets. An increase in Sm/Nd of 2% can result in a planetary embryo with a ^{142}Nd excess of some 5ppm, or about half the difference between the Earth and enstatite chondrites (Burkhardt et al., 2016). We note that the degree of depletion of Nd relative to Sm in our model crust depends on the partition coefficients and degree of melting used in the calculation. The ~2% depletion of Nd relative to Sm using our model crust shown in Figure 8 is based on conservative bulk partition coefficients using a composition in which partitioning is controlled by clinopyroxene, appropriate for small bodies with mantle interiors with pressures < 2 GPa. Using more extreme ratios, for example those expected if a significant amount of garnet is residual in the source rock, increases this relative Nd depletion. Indeed, using a KREEP-rich crust composition, embryos evolve with a ~4% depletion of Nd relative to Sm (Figure 8) which can account for the full difference in $^{142}Nd/^{144}Nd$ between the Earth and enstatite chondrites (Burkhardt et al., 2016).

O'Neill and Palme (2008) performed a simplistic version of the crust stripping calculation, constraining the amount of crust lost by the 6% increase in the Sm/Nd ratio perceived to be required to produce the 20 ppm ^{142}Nd excess reported by Boyet and Carlson (2005) in the original exposition of this problem. They found that this required 54% loss of a proto-crust formed by a low degree of melting, 2.6%. Such a low value was rationalised in relation to current day crustal fractions on Earth, but is rather small for typical estimates of planetesimal crusts. Given the discussion below, however, we have not investigated in further detail the parameter space controlling the exact magnitude of the values produced by loss of our 'model' crust.

Recent measurements have demonstrated that the Earth's ^{142}Nd anomaly is likely nucleosynthetic in origin (Burkhardt et al., 2016; Bouvier and Boyet, 2016),

and so a chondritic Sm/Nd for the Earth is again preferred, as has previously been argued (Huang et al., 2013). Near chondritic Sm/Nd is reproduced in our simulations if the proto-crust has a composition similar to eucrites, for which we find a small change in Sm/Nd from collisional erosion to a value less than 0.5% above the chondritic value. This small increase in the Sm/Nd ratio would be consistent with the current interpretation of terrestrial ^{142}Nd.

A longer standing concern over apparently non-chondritic refractory lithophile element abundances in bulk Earth has stemmed from coupled ^{143}Nd/^{144}Nd and ^{176}Hf/^{177}Hf measurements. The array of mantle values for these combined isotopic systems does not pass through the 'chondritic cross-hair' (ϵ^{143}Nd, ϵ^{176}Hf = 0, 0; Blichert-Toft and Albarède, 1997, where the ϵ notation indicates parts per ten thousand variation of the ^{143}Nd/^{144}Nd and ^{176}Hf/^{177}Hf ratios respectively from a chondritic reference), see Figure 9. This may simply reflect that the samples defining the mantle array contain variable contributions of subducted crustal components (e.g. oceanic crust and sediments) rather than primitive mantle and so might not be expected to pass through a chondritic composition. Yet it has subsequently become clear that many crustal samples define a similar array that has radiogenic Hf compositions at chondritic ^{143}Nd/^{144}Nd (Vervoort et al., 2011). Moreover, if a reconstituted bulk Earth is calculated by mixing depleted upper mantle, as represented by the source of mid-ocean ridge basalts, with average continental crust, the mixing array is convex upwards and has positive ϵ^{176}Hf at ϵ^{143}Nd = 0 (see Figure 9). Accessible samples of the Earth are therefore not readily combined to reproduce a bulk chondritic composition (Blichert-Toft and Albarède, 1997). This led to the suggestion of a hidden reservoir at the base of the mantle (Walter and Trønnes, 2004) as was subsequently used as explanation for elevated terrestrial ^{142}Nd (Labrosse et al., 2007). Less exotically, the lower continental crust might be a suitable complementary reservoir. Whilst accretional erosion has been invoked to account for elevated ^{142}Nd, to our knowledge, this process has not been explored for its influence on terrestrial ^{143}Nd/^{144}Nd and ^{176}Hf/^{177}Hf systematics.

In contrast to the Sm-Nd case, loss of eucritic crust produces significant Lu-Hf fractionations. Thus accretional erosion of eucritic, model or KREEP-rich crust will result in planetary embryos with super-chondritic Lu/Hf (Figure 8) that evolve into positive modern ϵ^{176}Hf (deviations in ^{176}Hf/^{177}Hf above chondrite, see Figure 9 and Appendix B). Predicted embryo compositions largely lie within the bounds of the terrestrial Nd-Hf
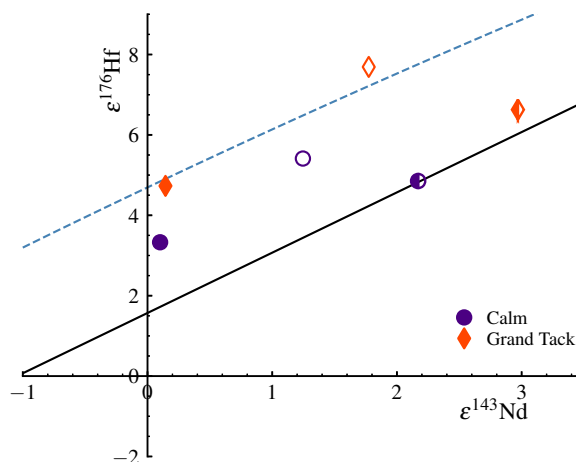
Figure 9: Nd-Hf systematics of the Earth and collisionally processed embryos. The solid black line represents the best fit terrestrial array from Vervoort et al. (2011); the blue dashed line represents a continental crust-depleted mantle mixing array. The former was assumed to have ϵ^{176}Hf=-13 and ϵ^{143}Nd=-10 (taken from sedimentary analyses from Vervoort et al. 2011) and [Nd]=20 and [Hf]=3.7 (Rudnick and Fountain, 1995) while the latter was taken to have ϵ^{176}Hf=16.8 and ϵ^{143}Nd=9.8 with [Nd]=0.581 and [Hf]=0.157 (Workman and Hart, 2005). In the absence of a hidden reservoir, values for bulk silicate earth are expected to fall somewhere within these arrays, as is the case for our calculated planetary embryo compositions. Filled symbols represent bulk Earth after stripping of a eucritic crust, open symbols correspond to stripping of our model crust, and half-filled symbols correspond to stripping of a KREEP-rich crust.

isotopic crust-mantle array (Vervoort et al., 2011) and mantle-crust mixing curve Figure 9, although loss of KREEP-rich crust results in an extreme composition both in terms of ϵ^{176}Hf and ϵ^{143}Nd. Assuming a nucleosynthetic origin for ^{142}Nd excesses on Earth, we favour a scenario with loss of eucritic crust, as this will not produce associated radiogenic ^{142}Nd anomalies. Hence, we suggest that the Nd-Hf systematics of the Earth can be generated by crustal erosion of Vesta-like bodies during accretion. This implies that the heat producing budget of the Earth is ~20% depleted relative to its initial chondritic protolith (Figure 7).

5. Summary

We have conducted smoothed particle hydrodynamics simulations of collisions between differentiated rocky planetesimals and planetary embryos to examine the stripping of planetary crusts during accretion of embryos. We found the largest remnant mass to be consistent with the Leinhardt and Stewart (2012) scaling law in this intermediate size regime. These simulations show that crust is preferentially lost during impacts, and we have developed a scaling law for crust ejection. Using this scaling law and the *N*-body simulations of terrestrial planet formation from Carter et al. (2015), we have estimated the maximum effect of collisions during accretion on incompatible element abundances in planetary embryos.

We find that collisional erosion of proto-crust can lower the budgets of the heat producing elements by ~20%. However, if reaccretion of lost material is very efficient this would substantially reduce any compositional modifications due to collisional erosion, though some variation between planetary bodies would still be likely.

If the composition of proto-crust is similar to the eucrites, planetary Nd isotope ratios remain chondritic; however, alternative crustal compositions can raise Sm/Nd ratios, leading to non-chondritic ^{142}Nd/^{144}Nd, which would be inconsistent with recent inferences (Burkhardt et al., 2016; Bouvier and Boyet, 2016). We find that the Lu-Hf system is notably fractionated even with a eucrite-like crust, which can result in a superchondritic ^{176}Hf/^{177}Hf with chondritic ^{143}Nd/^{144}Nd, in keeping with the inferred composition of Earth.

We have shown that stripping of planetary crusts during accretion can lead to noticeable changes in bulk composition of lithophile elements, but the fractionation is subtle, and sensitive to the unknown efficiency of reaccretion of the stripped material.

Appendix A. Crustal compositions

In the post-processing calculations we use Vesta as a suitable analogue for intermediate sized planetesimals, and consider three different approaches for setting crustal compositions.

For the 'model' Vestan crust we use a simplified model of crust formation based on petrological models discussed in Ruzicka et al. (1997) and Mandler and Elkins-Tanton (2013). We assume the crust is formed as a 20% melt fraction (i.e. the crust mass is 20% of the silicate mass of the body, ~15% of the total mass), which is appropriate for the estimated fraction of eucritic crust. We use a bulk silicate Vesta composition from Ruzicka et al. (1997), which estimates 3×CI chondrite abundances for the refractory lithophile elements studied here, see Table 1. (Chondritic meteorites provide a reliable reference for the ratios of refractory elements, and as lithophile elements, the influence of core formation on element ratios is also insignificant, even if the absolute abundances of the elements require independent estimation). For calculating the composition of a 20% melt from bulk silicate Vesta, we use the self-consistent set of bulk partition coefficients reported in Workman and Hart (2005) which mimic approximately similar conditions. The calculations are insensitive to the exact values of partition coefficients used, given their low values for all elements considered relative to the melt fraction. We also note that the batch partitioning scenario we consider can represent either the residue of magma ocean crystallisation (as in Ruzicka et al. 1997 and Mandler and Elkins-Tanton 2013) or partial mantle melts, as envisioned for Vesta by Stolper (1977) or for the terrestrial situation modelled by Workman and Hart (2005).

In addition to the 'model' crust we use analyses of eucrites as a direct sample of Vestan crust. Given our

focus on Sm-Nd and Lu-Hf, we use the high-precision, isotope dilution dataset from Blichert-Toft et al. (2002). For Th and U concentrations we take the average values from Barrat et al. (2000), renormalized so that the mean [Nd] of these data equal the mean [Nd] of the Blichert-Toft et al. (2002) data. As for the model crust we assume this empirical 'eucritic' crust is 20% of the silicate mass.

The incompatible element enrichment in eucritic samples is modest. More extreme increases in incompatible element abundances and fractionations of one element to another is evident in the final residual liquid of lunar crystallisation, the so-called KREEP layer. This reflects an endmember scenario for differentiation of a larger body. The high-K KREEP composition of Warren (1989), corresponds to a ~0.4% residual liquid of lunar magma ocean crystallisation (Snyder et al., 1992). This incompatible element enriched layer does not form the crust itself but in an idealised lunar stratigraphy lies beneath the flotation anorthosite crust. Thus, removal of KREEP will occur with simultaneous removal of this overlying plagioclase unit which contains low abundances of the incompatible elements of interest. We have therefore calculated a 'crustal' composition that averages a KREEP layer that is 0.375% of lunar mass with anorthosite representing 4.66% of lunar mass (Wieczorek et al., 2013). We use elemental abundances for average high-K KREEP from Warren (1989) and for the anorthosite using the 'enriched' sample 15415 from Münker (2010). For the latter there are no Th nor U concentration data and we assume that the contents of these highly incompatible elements are negligible. For consistency with lunar crystallisation, we assume this 'KREEP-rich' crust represents 5.04% of a body's silicate mass.

Appendix B. Isotope calculations

The deviations in present day ^{142}Nd/^{144}Nd, ^{143}Nd/^{144}Nd and ^{176}Hf/^{177}Hf from a chondritic reference are calculated from our collisionally processed Sm/Nd and Lu/Hf ratios assuming an age of 4.567 Gyr. The present day chondritic ratios of ^{142}Nd/^{144}Nd and ^{146}Sm/^{144}Nd were obtained from Caro et al. (2003), and the present day chondritic ratios of ^{143}Nd/^{144}Nd, ^{176}Hf/^{177}Hf, ^{147}Sm/^{144}Nd, and ^{176}Lu/^{177}Hf were taken from Bouvier et al. (2008). The half lives of ^{147}Sm, $t_{1/2} = 1.06 \times 10^{11}$ yr, and ^{176}Lu, $t_{1/2} = 3.71 \times 10^{10}$ yr, were taken from Begemann et al. (2001) and Scherer et al. (2001).

Supplementary material

Table S1: Summary of parameters and results of simulated collisions.

Table S2: Summary of results for second largest remnant of hit-and-run collisions.

Figure S1: Comparison of processed embryo abundances between different crust formation scenarios.

Animations to accompany Figure 4.

References

References

Adachi, I., Hayashi, C., Nakazawa, K., Dec. 1976. The gas drag effect on the elliptical motion of a solid body in the primordial solar nebula. Progress of Theoretical Physics 56, 1756–1771. 4.2

Amelin, Y., Jan. 2008. U Pb ages of angrites. Geochim. Cosmochim. Acta72, 221–232. 1

Barrat, J. A., Blichert-Toft, J., Gillet, P., Keller, F., Sep. 2000. The differentiation of eucrites: The role of in situ crystallization. Meteoritics and Planetary Science 35, 1087–1100. 2.2, 1, Appendix A

Begemann, F., Ludwig, K. R., Lugmair, G. W., Min, K., Nyquist, L. E., Patchett, P. J., Renne, P. R., Shih, C.-Y., Villa, I. M., Walker, R. J., Jan. 2001. Call for an improved set of decay constants for geochronological use. Geochim. Cosmochim. Acta65, 111–121. Appendix B

Bizzarro, M., Baker, J. A., Haack, H., Lundgaard, K. L., Oct. 2005. Rapid Timescales for Accretion and Melting of Differentiated Planetesimals Inferred from ^{26}Al-^{26}Mg Chronometry. ApJ632, L41–L44. 1

Blichert-Toft, J., Albarède, F., Apr. 1997. The Lu-Hf isotope geochemistry of chondrites and the evolution of the mantle-crust system. Earth and Planetary Science Letters 148, 243–258. 4.2

Blichert-Toft, J., Boyet, M., Télouk, P., Albarède, F., Nov. 2002. ^{147}Sm- ^{143}Nd and ^{176}Lu- ^{176}Hf in eucrites and the differentiation of the HED parent body. Earth and Planetary Science Letters 204, 167–181. 2.2, 1, Appendix A, Appendix A

Bonsor, A., Leinhardt, Z. M., Carter, P. J., Elliott, T., Walter, M. J., Stewart, S. T., Feb. 2015. A collisional origin to Earth's non-chondritic composition? Icarus247, 291–300. 1, 1.1, 3.1, 3.2

Boujibar, A., Andrault, D., Bolfan-Casanova, N., Bouhifd, M. A., Monteux, J., 09 2015. Cosmochemical fractionation by collisional erosion during the earth's accretion. Nature Communications 6, 8295 EP –.
URL http://dx.doi.org/10.1038/ncomms9295 1, 4.2

Bourdon, B., Touboul, M., Caro, G., Kleine, T., Nov. 2008. Early differentiation of the Earth and the Moon. Royal Society of London Philosophical Transactions Series A 366, 4105–4128. 1

Bouvier, A., Boyet, M., Sep. 2016. Primitive Solar System materials and Earth share a common initial ^{142}Nd abundance. Nature537, 399–402. 1, 4.2, 5

Bouvier, A., Vervoort, J. D., Patchett, P. J., Aug. 2008. The Lu-Hf and Sm-Nd isotopic composition of CHUR: Constraints from unequilibrated chondrites and implications for the bulk composition of terrestrial planets. Earth and Planetary Science Letters 273, 48–57. Appendix B

Boyet, M., Carlson, R. W., Jul. 2005. ^{142}Nd Evidence for Early (>4.53 Ga) Global Differentiation of the Silicate Earth. Science 309, 576–581. 1, 4.2

Burkhardt, C., Borg, L. E., Brennecka, G. A., Shollenberger, Q. R., Dauphas, N., Kleine, T., Sep. 2016. A nucleosynthetic origin for the Earth's anomalous [142]Nd composition. Nature537, 394–398. 1, 4.2, 5

Caro, G., Bourdon, B., Birck, J.-L., Moorbath, S., May 2003. [146]Sm-[142]Nd evidence from Isua metamorphosed sediments for early differentiation of the Earth's mantle. Nature423, 428–432. Appendix B

Carter, P. J., Leinhardt, Z. M., Elliott, T., Walter, M. J., Stewart, S. T., Nov. 2015. Compositional Evolution during Rocky Proto-planet Accretion. ApJ813, 72. 1, 1.1, 2.1, 2.2, 3.1, 3.2, 3.2, 7, 8, 4.1, 4.2, 5

Ćuk, M., Stewart, S. T., Nov. 2012. Making the Moon from a Fast-Spinning Earth: A Giant Impact Followed by Resonant Despinning. Science 338, 1047–. 2.1

Dwyer, C. A., Nimmo, F., Chambers, J. E., Jan. 2015. Bulk chemical and Hf-W isotopic consequences of incomplete accretion during planet formation. Icarus245, 145–152. 1

Fujiwara, A., Kamimoto, G., Tsukamoto, A., Jun. 1977. Destruction of basaltic bodies by high-velocity impact. Icarus31, 277–288. 2

Genda, H., Fujita, T., Kobayashi, H., Tanaka, H., Abe, Y., Dec. 2015. Resolution dependence of disruptive collisions between planetesimals in the gravity regime. Icarus262, 58–66. 4.1

Greenwood, R. C., Franchi, I. A., Jambon, A., Buchanan, P. C., 06 2005. Widespread magma oceans on asteroidal bodies in the early solar system. Nature 435 (7044), 916–918.
URL http://dx.doi.org/10.1038/nature03612 1

Hevey, P. J., Sanders, I. S., Jan. 2006. A model for planetesimal melt-down by [26]Al and its implications for meteorite parent bodies. Meteoritics and Planetary Science 41, 95–106. 2.1

Hin, R. C., Coath, C. D., Carter, P. J., Nimmo, F., Lai, Y.-J., Pogge von Strandmann, P. A. E., Willbold, M., Leinhardt, Z. M., Walter, M. J., Elliott, T., Sep. 2017. Magnesium isotope evidence that accretional vapour loss shapes planetary compositions. Nature549, 511–515. 4.2

Huang, S., Jacobsen, S. B., Mukhopadhyay, S., 2013. 147sm-143nd systematics of earth are inconsistent with a superchondritic sm/nd ratio. Proceedings of the National Academy of Sciences 110 (13), 4929–4934.
URL http://www.pnas.org/content/110/13/4929.abstract 1, 4.2

Jellinek, A. M., Jackson, M. G., Aug. 2015. Connections between the bulk composition, geodynamics and habitability of Earth. Nature Geoscience 8, 587–593. 1

Kobayashi, H., Tanaka, H., Apr. 2010. Fragmentation model dependence of collision cascades. Icarus206, 735–746. 4.2

Kruijer, T. S., Touboul, M., Fischer-Gödde, M., Bermingham, K. R., Walker, R. J., Kleine, T., Jun. 2014. Protracted core formation and rapid accretion of protoplanets. Science 344, 1150–1154. 1

Labrosse, S., Hernlund, J. W., Coltice, N., Dec. 2007. A crystallizing dense magma ocean at the base of the Earth's mantle. Nature450, 866–869. 1, 4.2

Leinhardt, Z. M., Dobinson, J., Carter, P. J., Lines, S., Jun. 2015. Numerically Predicted Indirect Signatures of Terrestrial Planet Formation. ApJ806, 23. 1.1

Leinhardt, Z. M., Stewart, S. T., Jan. 2012. Collisions between Gravity-dominated Bodies. I. Outcome Regimes and Scaling Laws. ApJ745, 79. 1, 1.1, 2, 2.1, 2.2, 2, 3.1, 4.1, 5

Lock, S. J., Stewart, S. T., May 2017. The structure of terrestrial bodies: Impact heating, corotation limits, and synestias. Journal of Geophysical Research (Planets) 122, 950–982. 2.1

Lugmair, G. W., Shukolyukov, A., Aug. 1998. Early solar system timescales according to [53]Mn- [53]Cr systematics. Geochim. Cosmochim. Acta62, 2863–2886. 1

Mandler, B. E., Elkins-Tanton, L. T., Nov. 2013. The origin of eu-

crites, diogenites, and olivine diogenites: Magma ocean crystallization and shallow magma chamber processes on Vesta. Meteoritics and Planetary Science 48, 2333–2349. 2.2, Appendix A, Appendix A

Marcus, R. A., Sasselov, D., Stewart, S. T., Hernquist, L., Aug. 2010. Water/Icy Super-Earths: Giant Impacts and Maximum Water Content. ApJ719, L45–L49. 1, 1.1, 2.1

Marcus, R. A., Stewart, S. T., Sasselov, D., Hernquist, L., Aug. 2009. Collisional Stripping and Disruption of Super-Earths. ApJ700, L118–L122. 1, 1.1, 2.1, 2.1, 3.1, 3, 3.1, 4.1

Marinova, M. M., Aharonson, O., Asphaug, E., Jun. 2008. Mega-impact formation of the Mars hemispheric dichotomy. Nature453, 1216–1219. 2.1

Meissner, F., Schmidt-Ott, W. D., Ziegeler, L., Jun 1987. Half-life and α-ray energy of146sm. Zeitschrift für Physik A Atomic Nuclei 327 (2), 171–174.
URL https://doi.org/10.1007/BF01292406 1

Melosh, H. J., 2007. A hydrocode equation of state for SiO2. Meteoritics and Planetary Science 42, 2079–2098. 2.1

Morbidelli, A., Lunine, J. I., O'Brien, D. P., Raymond, S. N., Walsh, K. J., May 2012. Building Terrestrial Planets. Annual Review of Earth and Planetary Sciences 40, 251–275. 1

Münker, C., Dec. 2010. A high field strength element perspective on early lunar differentiation. Geochim. Cosmochim. Acta74, 7340–7361. 1, Appendix A

O'Neill, H. S. C., Palme, H., Nov. 2008. Collisional erosion and the non-chondritic composition of the terrestrial planets. Royal Society of London Philosophical Transactions Series A 366, 4205–4238. 1, 4.2

Palme, H., Jones, A., Dec. 2003. Solar System Abundances of the Elements. Treatise on Geochemistry 1, 41–61. 1

Pringle, E. A., Moynier, F., Savage, P. S., Badro, J., Barrat, J.-A., 2014. Silicon isotopes in angrites and volatile loss in planetesimals. Proceedings of the National Academy of Sciences 111 (48), 17029–17032.
URL http://www.pnas.org/content/111/48/17029.abstract 4.2

Rudnick, R. L., Fountain, D. M., 1995. Nature and composition of the continental crust: A lower crustal perspective. Reviews of Geophysics 33, 267–310. 9

Ruzicka, A., Snyder, G. A., Taylor, L. A., Nov. 1997. Vesta as the HED Parent Body: Implications for the Size of a Core and for Large-Scale Differentiation. Meteoritics and Planetary Science 32. 2.2, Appendix A, Appendix A, Appendix A

Scherer, E., Münker, C., Mezger, K., Jul. 2001. Calibration of the Lutetium-Hafnium Clock. Science 293, 683–687. Appendix B

Snyder, G. A., Taylor, L. A., Neal, C. R., Oct. 1992. A chemical model for generating the sources of mare basalts - Combined equilibrium and fractional crystallization of the lunar magmasphere. Geochim. Cosmochim. Acta56, 3809–3823. 2.2, Appendix A

Springel, V., Dec. 2005. The cosmological simulation code GADGET-2. MNRAS364, 1105–1134. 2.1

Srinivasan, G., Goswami, J. N., Bhandari, N., May 1999. 26Al in Eucrite Piplia Kalan: Plausible Heat Source and Formation Chronology. Science 284, 1348. 1

Stewart, S. T., Leinhardt, Z. M., May 2012. Collisions between Gravity-dominated Bodies. II. The Diversity of Impact Outcomes during the End Stage of Planet Formation. ApJ751, 32. 4.2

Stolper, E., May 1977. Experimental petrology of eucritic meteorites. Geochim. Cosmochim. Acta41, 587–611. Appendix A

Vervoort, J. D., Plank, T., Prytulak, J., Oct. 2011. The Hf-Nd isotopic composition of marine sediments. Geochim. Cosmochim. Acta75, 5903–5926. 4.2, 9, 4.2

Walsh, K. J., Morbidelli, A., Raymond, S. N., O'Brien, D. P., Mandell, A. M., Jul. 2011. A low mass for Mars from Jupiter's early gas-

driven migration. Nature475, 206–209. 1.1

Walter, M. J., Trønnes, R. G., Sep. 2004. Early Earth differentiation [rapid communication]. Earth and Planetary Science Letters 225, 253–269. 4.2

Warren, P. H., 1989. KREEP: major-element diversity, trace-element uniformity (almost). In: Taylor, G. J., Warren, P. H. (Eds.), Moon in Transition: Apollo 14, KREEP, and Evolved Lunar Rocks. pp. 149–153. 1, Appendix A, Appendix A

Wieczorek, M. A., Neumann, G. A., Nimmo, F., Kiefer, W. S., Taylor, G. J., Melosh, H. J., Phillips, R. J., Solomon, S. C., Andrews-Hanna, J. C., Asmar, S. W., Konopliv, A. S., Lemoine, F. G., Smith, D. E., Watkins, M. M., Williams, J. G., Zuber, M. T., Feb. 2013. The Crust of the Moon as Seen by GRAIL. Science 339, 671–675. Appendix A

Workman, R. K., Hart, S. R., Feb. 2005. Major and trace element composition of the depleted MORB mantle (DMM). Earth and Planetary Science Letters 231, 53–72. 2.2, 1, 9, Appendix A, Appendix A

Table S1: Summary of parameters and results of simulated collisions.
$f_{\mathrm{Fe,lr}} = M_{\mathrm{Fe}}/M_{\mathrm{lr}}$, $f_{\mathrm{crust,lr}} = M_{\mathrm{crust}}/M_{\mathrm{lr}}$

M_{targ} ($M_\oplus$)	mass ratio	b	v (km s^{-1})	N_{targ}	R_{targ} (km)	R_{proj} (km)	Q_{R} (J kg^{-1})	Q'^{*}_{RD} (J kg^{-1})	$M_{\mathrm{lr}}/M_{\mathrm{Tot}}$	$f_{\mathrm{Fe,lr}}$	$f_{\mathrm{crust,lr}}$	$M_{\mathrm{slr}}/M_{\mathrm{Tot}}$
1e-05	1.00	0.40	0.28	19999	148	148	9.65e+03	2.88e+04	0.99	0.21	0.14	-
1e-05	1.00	0.40	0.36	19999	148	148	1.63e+04	2.88e+04	0.94	0.23	0.13	-
1e-05	1.00	0.40	0.42	19999	148	148	2.17e+04	2.88e+04	0.44	0.24	0.12	0.43
1e-05	1.00	0.40	0.56	19999	148	148	3.86e+04	2.88e+04	0.33	0.31	0.11	0.33
1e-05	1.00	0.40	0.69	19999	148	148	6.03e+04	2.88e+04	0.27	0.37	0.10	0.27
1e-05	1.00	0.40	0.83	19999	148	148	8.68e+04	2.88e+04	0.23	0.38	0.09	0.23
1e-05	1.00	0.40	4.17	19999	148	148	2.17e+06	2.88e+04	-*	-	-	-
1e-05	1.00	0.80	0.66	19999	148	148	5.49e+04	5.36e+05	0.47†	0.22	0.14	0.47
1e-05	1.00	0.80	0.80	19999	148	148	7.91e+04	5.36e+05	0.46*†	0.23	0.13	0.46
5e-05	0.20	0.40	0.81	19999	252	147	4.58e+04	3.61e+05	0.81	0.23	0.13	0.02
5e-05	0.20	0.40	1.22	19999	252	147	1.03e+05	3.61e+05	0.69	0.26	0.12	-
5e-05	0.20	0.40	2.44	19999	252	147	4.12e+05	3.61e+05	0.46	0.37	0.10	-
5e-05	0.20	0.40	4.87	19999	252	147	1.65e+06	3.61e+05	0.02*	0.37	0.09	0.02
5e-05	0.20	0.80	0.33	19999	252	147	7.39e+03	5.39e+05	1.00	0.21	0.15	-
5e-05	0.20	0.80	0.82	19999	252	147	5.94e+04	5.39e+05	0.83†	0.21	0.15	0.14
5e-05	0.20	0.80	1.22	19999	252	147	1.34e+05	5.39e+05	0.82†	0.22	0.14	0.12
5e-05	0.20	0.80	2.45	19999	252	147	5.34e+05	5.39e+05	0.79†	0.22	0.14	0.08
5e-05	0.30	0.10	0.33	19999	252	169	9.76e+03	1.21e+05	1.00	0.21	0.15	-
5e-05	0.30	0.10	0.50	19999	252	169	2.20e+04	1.21e+05	0.98	0.22	0.14	-
5e-05	0.30	0.10	0.50	199999	259	174	2.20e+04	1.21e+05	0.95	0.22	0.12	-
5e-05	0.30	0.10	1.04	19999	252	169	9.53e+04	1.21e+05	0.61	0.35	0.10	-
5e-05	0.30	0.10	1.04	199999	259	174	9.53e+04	1.21e+05	0.56	0.34	0.09	0.00
5e-05	0.30	0.10	1.24	19999	252	169	1.37e+05	1.21e+05	0.47	0.40	0.09	-
5e-05	0.30	0.10	1.87	19999	252	169	3.09e+05	1.21e+05	0.05	0.46	0.09	0.03
5e-05	0.30	0.10	1.87	199999	259	174	3.09e+05	1.21e+05	0.06*	0.32	0.09	0.02
5e-05	0.30	0.10	3.73	19999	252	169	1.24e+06	1.21e+05	-*	-	-	-
5e-05	0.30	0.25	0.33	19999	252	169	9.89e+03	1.23e+05	1.00	0.21	0.15	-
5e-05	0.30	0.25	0.50	19999	252	169	2.23e+04	1.23e+05	0.97	0.22	0.14	-
5e-05	0.30	0.25	0.50	199999	259	174	2.23e+04	1.23e+05	0.94	0.23	0.12	-
5e-05	0.30	0.25	1.04	19999	252	169	9.66e+04	1.23e+05	0.59	0.30	0.11	0.06
5e-05	0.30	0.25	1.04	199999	259	174	9.66e+04	1.23e+05	0.57*	0.30	0.10	0.05
5e-05	0.30	0.25	1.25	19999	252	169	1.39e+05	1.23e+05	0.47	0.34	0.10	0.02
5e-05	0.30	0.25	1.88	19999	252	169	3.13e+05	1.23e+05	0.29	0.39	0.09	0.01
5e-05	0.30	0.25	1.88	199999	259	174	3.13e+05	1.23e+05	0.28*	0.37	0.08	0.00
5e-05	0.30	0.25	3.76	19999	252	169	1.25e+06	1.23e+05	0.01*	0.36	0.10	0.01
5e-05	0.30	0.40	0.33	19999	252	169	9.96e+03	2.47e+05	1.00	0.21	0.15	-
5e-05	0.30	0.40	0.50	19999	252	169	2.24e+04	2.47e+05	0.95	0.22	0.14	0.01
5e-05	0.30	0.40	1.05	19999	252	169	9.72e+04	2.47e+05	0.63	0.26	0.12	0.05
5e-05	0.30	0.40	1.88	19999	252	169	3.15e+05	2.47e+05	0.42	0.37	0.10	-
5e-05	0.30	0.40	3.77	19999	252	169	1.26e+06	2.47e+05	0.14	0.39	0.09	0.00
5e-05	0.30	0.40	6.28	19999	252	169	3.50e+06	2.47e+05	-*	-	-	-
5e-05	0.30	0.50	0.34	19999	252	169	9.97e+03	2.72e+05	1.00	0.21	0.15	-
5e-05	0.30	0.50	0.50	19999	252	169	2.24e+04	2.72e+05	0.94	0.23	0.14	0.01
5e-05	0.30	0.50	0.50	199999	259	174	2.24e+04	2.72e+05	0.92	0.23	0.13	0.01
5e-05	0.30	0.50	1.05	19999	252	169	9.73e+04	2.72e+05	0.67	0.25	0.12	0.03
5e-05	0.30	0.50	1.05	199999	259	174	9.73e+04	2.72e+05	0.66*	0.25	0.12	0.02
5e-05	0.30	0.50	1.26	19999	252	169	1.40e+05	2.72e+05	0.62	0.26	0.12	0.01
5e-05	0.30	0.50	1.88	19999	252	169	3.15e+05	2.72e+05	0.49	0.33	0.10	-
5e-05	0.30	0.50	1.88	199999	259	174	3.15e+05	2.72e+05	0.46*	0.35	0.09	0.00

Table S1: Summary of parameters and results of simulated collisions.
$f_{\mathrm{Fe,lr}} = M_{\mathrm{Fe}}/M_{\mathrm{lr}}$, $f_{\mathrm{crust,lr}} = M_{\mathrm{crust}}/M_{\mathrm{lr}}$

M_{targ} ($\mathrm{M_\oplus}$)	mass ratio	b	v ($\mathrm{km\,s^{-1}}$)	N_{targ}	R_{targ} (km)	R_{proj} (km)	Q_{R} ($\mathrm{J\,kg^{-1}}$)	Q'^{*}_{RD} ($\mathrm{J\,kg^{-1}}$)	$M_{\mathrm{lr}}/M_{\mathrm{Tot}}$	$f_{\mathrm{Fe,lr}}$	$f_{\mathrm{crust,lr}}$	$M_{\mathrm{slr}}/M_{\mathrm{Tot}}$
5e-05	0.30	0.50	3.77	19999	252	169	1.26e+06	2.72e+05	0.26	0.36	0.09	-
5e-05	0.30	0.80	0.33	19999	252	169	9.87e+03	3.19e+05	1.00	0.21	0.15	-
5e-05	0.30	0.80	0.50	19999	252	169	1.96e+04	3.19e+05	0.79†	0.21	0.15	0.20
5e-05	0.30	0.80	1.04	19999	252	169	8.51e+04	3.19e+05	0.75†	0.22	0.14	0.18
5e-05	0.30	0.80	1.88	19999	252	169	2.76e+05	3.19e+05	0.72†	0.23	0.13	0.13
5e-05	0.50	0.40	0.53	19999	252	200	3.08e+04	2.27e+05	0.95	0.23	0.14	-
5e-05	0.50	0.40	1.10	19999	252	200	1.34e+05	2.27e+05	0.51	0.28	0.11	0.14
5e-05	0.50	0.40	1.75	19999	252	200	3.42e+05	2.27e+05	0.35	0.38	0.09	0.01
5e-05	0.50	0.40	6.58	19999	252	200	4.81e+06	2.27e+05	-*	-	-	-
5e-05	0.50	0.80	0.34	19999	252	200	1.32e+04	6.79e+05	0.99	0.22	0.15	0.01
5e-05	0.50	0.80	0.52	19999	252	200	1.74e+04	6.79e+05	0.67†	0.21	0.15	0.31
5e-05	0.50	0.80	1.08	19999	252	200	7.57e+04	6.79e+05	0.65†	0.22	0.14	0.30
5e-05	0.50	0.80	2.58	19999	252	200	4.36e+05	6.79e+05	0.60†	0.24	0.13	0.22
1e-03	0.02	0.40	2.00	199999	702	190	3.84e+04	1.92e+06	0.99	0.22	0.14	-
1e-03	0.02	0.40	3.00	199999	702	190	8.64e+04	1.92e+06	0.98	0.22	0.14	-
1e-03	0.02	0.40	8.99	199999	702	190	7.77e+05	1.92e+06	0.77*	0.27	0.11	0.00
1e-03	0.02	0.40	11.99	199999	702	190	1.38e+06	1.92e+06	0.59*	0.36	0.06	0.00
1e-03	0.02	0.40	14.99	199999	702	190	2.16e+06	1.92e+06	0.47*	0.44	0.03	0.00
1e-03	0.02	0.80	2.04	199999	702	190	5.12e+05	9.52e+05	0.98†	0.22	0.15	-
1e-03	0.02	0.80	3.05	199999	702	190	1.15e+06	9.52e+05	0.98†	0.22	0.15	-
1e-03	0.02	0.80	9.16	199999	702	190	1.04e+07	9.52e+05	0.96*†	0.22	0.14	-
1e-03	0.05	0.40	0.82	199999	702	258	1.53e+04	2.00e+06	1.00	0.22	0.15	-
1e-03	0.05	0.40	1.13	199999	702	258	2.89e+04	2.00e+06	0.99	0.22	0.15	-
1e-03	0.05	0.40	2.05	199999	702	258	9.56e+04	2.00e+06	0.97	0.22	0.14	-
1e-03	0.05	0.40	9.24	199999	702	258	1.94e+06	2.00e+06	0.49*	0.41	0.06	0.00
1e-03	0.05	0.40	10.27	199999	702	258	2.39e+06	2.00e+06	0.43*	0.45	0.05	0.01
1e-03	0.05	0.40	14.37	199999	702	258	4.68e+06	2.00e+06	0.17*	0.48	0.00	0.01
1e-03	0.05	0.80	0.84	199999	702	258	1.58e+04	9.34e+06	0.99	0.22	0.15	0.00
1e-03	0.05	0.80	2.09	199999	702	258	5.28e+05	1.47e+06	0.95†	0.22	0.14	0.01
1e-03	0.05	0.80	3.13	199999	702	258	1.19e+06	1.47e+06	0.95†	0.22	0.14	0.00
1e-03	0.10	0.10	2.07	19999	683	317	1.78e+05	1.34e+06	0.95	0.22	0.14	-
1e-03	0.10	0.10	5.71	19999	683	317	1.35e+06	1.34e+06	0.50	0.36	0.10	-
1e-03	0.10	0.10	7.78	19999	683	317	2.50e+06	1.34e+06	0.04*	0.32	0.10	0.02
1e-03	0.10	0.10	8.30	19999	683	317	2.85e+06	1.34e+06	0.03*	0.33	0.08	0.02
1e-03	0.10	0.10	9.85	19999	683	317	4.01e+06	1.34e+06	-*	-	-	-
1e-03	0.10	0.10	10.37	19999	683	317	4.45e+06	1.34e+06	-*	-	-	-
1e-03	0.10	0.25	2.10	19999	683	317	1.82e+05	1.46e+06	0.94	0.23	0.14	-
1e-03	0.10	0.25	5.77	19999	683	317	1.37e+06	1.46e+06	0.53	0.35	0.10	-
1e-03	0.10	0.25	7.87	19999	683	317	2.56e+06	1.46e+06	0.19	0.47	0.07	0.07
1e-03	0.10	0.25	8.39	19999	683	317	2.91e+06	1.46e+06	0.15*	0.47	0.07	0.06
1e-03	0.10	0.25	9.96	19999	683	317	4.10e+06	1.46e+06	0.03*	0.54	0.03	0.03
1e-03	0.10	0.25	10.49	19999	683	317	4.54e+06	1.46e+06	0.02*	0.47	0.01	0.02
1e-03	0.10	0.40	0.85	19999	683	317	2.96e+04	2.40e+06	1.00	0.22	0.15	-
1e-03	0.10	0.40	2.12	19999	683	317	1.85e+05	2.40e+06	0.93	0.23	0.14	-
1e-03	0.10	0.40	5.82	19999	683	317	1.40e+06	2.40e+06	0.62	0.31	0.11	-
1e-03	0.10	0.40	7.93	19999	683	317	2.60e+06	2.40e+06	0.48	0.39	0.09	0.01
1e-03	0.10	0.40	8.46	19999	683	317	2.96e+06	2.40e+06	0.41	0.43	0.08	0.01
1e-03	0.10	0.40	9.52	19999	683	317	3.74e+06	2.40e+06	0.23*	0.48	0.07	0.04
1e-03	0.10	0.40	10.05	19999	683	317	4.17e+06	2.40e+06	0.21	0.47	0.06	0.04

Table S1: Summary of parameters and results of simulated collisions.
$f_{\rm Fe,lr} = M_{\rm Fe}/M_{\rm lr}$, $f_{\rm crust,lr} = M_{\rm crust}/M_{\rm lr}$

$M_{\rm targ}$ (M$_\oplus$)	mass ratio	b	v (km s^{-1})	$N_{\rm targ}$	$R_{\rm targ}$ (km)	$R_{\rm proj}$ (km)	$Q_{\rm R}$ (J kg^{-1})	$Q'^*_{\rm RD}$ (J kg^{-1})	$M_{\rm lr}/M_{\rm Tot}$	$f_{\rm Fe,lr}$	$f_{\rm crust,lr}$	$M_{\rm slr}/M_{\rm Tot}$
1e-03	0.10	0.40	10.58	19999	683	317	4.62e+06	2.40e+06	0.19*	0.50	0.05	0.03
1e-03	0.10	0.80	2.14	19999	683	317	4.94e+05	1.43e+06	0.91†	0.21	0.15	0.05
1e-03	0.10	0.80	3.22	19999	683	317	1.11e+06	1.43e+06	0.90†	0.22	0.14	0.04
1e-03	0.10	0.80	5.90	19999	683	317	3.74e+06	1.43e+06	0.88*†	0.22	0.14	0.03
1e-03	0.40	0.40	2.33	19999	683	503	5.54e+05	1.45e+06	0.62	0.25	0.12	0.15
1e-03	0.40	0.40	4.66	19999	683	503	2.22e+06	1.45e+06	0.40	0.38	0.09	0.01
1e-03	0.40	0.40	6.99	19999	683	503	4.99e+06	1.45e+06	0.14	0.39	0.08	0.06
1e-03	0.40	0.40	8.74	19999	683	503	7.79e+06	1.45e+06	0.01	0.33	0.07	0.01
1e-03	0.40	0.40	9.32	19999	683	503	8.87e+06	1.45e+06	0.01	0.39	0.05	0.01
1e-03	0.40	0.40	9.90	19999	683	503	1.00e+07	1.45e+06	0.01	0.36	0.01	-
1e-03	0.40	0.40	10.49	19999	683	503	1.12e+07	1.45e+06	-	-	-	-
1e-03	0.40	0.80	2.30	19999	683	503	3.76e+05	3.65e+06	0.70†	0.22	0.14	0.25
1e-03	0.40	0.80	4.61	19999	683	503	1.50e+06	3.65e+06	0.68*†	0.23	0.14	0.21
1e-01	0.01	0.10	11.24	200000	3216	693	6.20e+05	4.34e+07	1.00	0.23	0.15	-
1e-01	0.01	0.10	17.99	200000	3216	693	1.59e+06	4.34e+07	0.99	0.23	0.14	-
1e-01	0.01	0.10	26.99	200000	3216	693	3.57e+06	4.34e+07	0.96*	0.24	0.14	-
1e-01	0.01	0.25	11.34	200000	3216	693	6.31e+05	4.06e+07	1.00	0.23	0.15	-
1e-01	0.01	0.25	18.15	200000	3216	693	1.61e+06	4.06e+07	0.99	0.23	0.14	-
1e-01	0.01	0.25	27.22	200000	3216	693	3.63e+06	4.06e+07	0.96*	0.24	0.13	-
1e-01	0.01	0.40	11.43	200000	3216	693	6.41e+05	3.50e+07	0.99	0.23	0.15	-
1e-01	0.01	0.40	18.29	200000	3216	693	1.64e+06	3.50e+07	0.99	0.23	0.14	-
1e-01	0.01	0.40	27.44	200000	3216	693	3.69e+06	3.50e+07	0.95*	0.24	0.13	-
1e-01	0.10	0.10	7.22	20000	3160	1466	2.16e+06	1.74e+07	0.98	0.23	0.14	-
1e-01	0.10	0.10	12.04	20000	3160	1466	5.99e+06	1.74e+07	0.89	0.25	0.13	-
1e-01	0.10	0.10	16.85	20000	3160	1466	1.17e+07	1.74e+07	0.64	0.34	0.09	-
1e-01	0.10	0.10	24.07	20000	3160	1466	2.39e+07	1.74e+07	0.31	0.59	0.01	-
1e-01	0.10	0.25	7.30	20000	3160	1466	2.20e+06	2.08e+07	0.97	0.23	0.14	-
1e-01	0.10	0.25	12.17	20000	3160	1466	6.12e+06	2.08e+07	0.88	0.26	0.13	-
1e-01	0.10	0.25	17.04	20000	3160	1466	1.20e+07	2.08e+07	0.68	0.31	0.11	-
1e-01	0.10	0.25	24.34	20000	3160	1466	2.45e+07	2.08e+07	0.43	0.47	0.04	-
1e-01	0.10	0.40	7.36	20000	3160	1466	2.24e+06	2.94e+07	0.96	0.23	0.14	-
1e-01	0.10	0.40	12.27	20000	3160	1466	6.22e+06	2.94e+07	0.86	0.25	0.13	0.00
1e-01	0.10	0.40	17.18	20000	3160	1466	1.22e+07	2.94e+07	0.77	0.27	0.12	-
1e-01	0.10	0.40	24.55	20000	3160	1466	2.49e+07	2.94e+07	0.58	0.35	0.09	-

* run time less than 24 hours.

† hit-and-run collision, $Q'^{\dagger*}_{\rm RD}$ is given. Largest remnant comes from the target, mass and composition of which are approximately unchanged. See Table S2 for remnant of projectile.

Table S2: Summary of results for second largest remnant of hit-and-run
collisions. $f_{\text{Fe,slr}} = M_{\text{Fe}}/M_{\text{slr}}$, $f_{\text{crust,slr}} = M_{\text{crust}}/M_{\text{slr}}$

M_{targ} (M$_\oplus$)	mass ratio	b	v (km s^{-1})	N_{targ}	R_{targ} (km)	R_{proj} (km)	$Q_{\text{R}}^{\dagger}$ (J kg^{-1})	$Q_{\text{RD}}^{\dagger\prime*}$ (J kg^{-1})	$M_{\text{slr}}/M_{\text{proj}}$	$f_{\text{Fe,slr}}$	$f_{\text{crust,slr}}$
1e-05	1.00	0.80	0.66	19999	148	148	5.49e+04	5.36e+05	0.94	0.22	0.14
1e-05	1.00	0.80	0.80	19999	148	148	7.91e+04	5.36e+05	0.92*	0.23	0.13
5e-05	0.20	0.80	0.82	19999	252	147	5.94e+04	5.39e+05	0.81	0.26	0.13
5e-05	0.20	0.80	1.22	19999	252	147	1.34e+05	5.39e+05	0.73	0.29	0.12
5e-05	0.20	0.80	2.45	19999	252	147	5.34e+05	5.39e+05	0.51	0.37	0.10
5e-05	0.30	0.80	0.50	19999	252	169	1.96e+04	3.19e+05	0.86	0.24	0.15
5e-05	0.30	0.80	1.04	19999	252	169	8.51e+04	3.19e+05	0.76	0.28	0.12
5e-05	0.30	0.80	1.88	19999	252	169	2.76e+05	3.19e+05	0.55	0.35	0.11
5e-05	0.50	0.80	0.52	19999	252	200	1.74e+04	6.79e+05	0.93	0.23	0.15
5e-05	0.50	0.80	1.08	19999	252	200	7.57e+04	6.79e+05	0.89	0.24	0.13
5e-05	0.50	0.80	2.58	19999	252	200	4.36e+05	6.79e+05	0.66	0.32	0.11
1e-03	0.02	0.80	2.04	199999	702	190	5.12e+05	9.52e+05	-	-	-
1e-03	0.02	0.80	3.05	199999	702	190	1.15e+06	9.52e+05	-	-	-
1e-03	0.02	0.80	9.16	199999	702	190	1.04e+07	9.52e+05	-*	-	-
1e-03	0.05	0.80	2.09	199999	702	258	5.28e+05	-	0.27‡	0.37	0.12
1e-03	0.05	0.80	3.13	199999	702	258	1.19e+06	-	0.04‡	0.38	0.12
1e-03	0.10	0.80	2.14	19999	683	317	4.94e+05	1.43e+06	0.60	0.33	0.12
1e-03	0.10	0.80	3.22	19999	683	317	1.11e+06	1.43e+06	0.49	0.38	0.11
1e-03	0.10	0.80	5.90	19999	683	317	3.74e+06	1.43e+06	0.32*	0.42	0.10
1e-03	0.40	0.80	2.30	19999	683	503	3.76e+05	3.65e+06	0.88	0.24	0.14
1e-03	0.40	0.80	4.61	19999	683	503	1.50e+06	3.65e+06	0.75*	0.28	0.12

* run time less than 24 hours.
‡ insufficient data to find $Q_{\text{RD}}^{\dagger\prime*}$, excluded from figures.